Large phonon-drag enhancement induced by narrow quantum confinement at the $LaAlO_3/SrTiO_3$ interface

I. Pallecchi,[1] F. Telesio,[1] D. Marré,[1] D. Li,[2] S. Gariglio,[2] J.-M. Triscone,[2] and A. Filippetti[3]
[1]*CNR-SPIN UOS Genova and Dipartimento di Fisica, Via Dodecaneso 33, 16146 Genova, Italy*
[2]*DQMP, University of Geneva, 24 Quai Ernest-Ansermet, 1211 Geneva 4, Switzerland*
[3]*CNR-IOM UOS Cagliari, S.P. Monserrato-Sestu Km.0,700, Monserrato (Ca) 09042, Italy*
(Received 3 March 2016; revised manuscript received 26 April 2016; published 12 May 2016)

The thermoelectric power of the two-dimensional electron system (2DES) at the $LaAlO_3/SrTiO_3$ interface is explored below room temperature, in comparison with that of Nb-doped $SrTiO_3$ single crystals. For the interface, we find a region below $T = 50$ K where thermopower is dominated by phonon drag, whose amplitude is hugely amplified with respect to the corresponding bulk value, reaching values ∼mV/K and above. The phonon-drag enhancement at the interface is traced back to the tight carrier confinement of the 2DES, and represents a sharp signature of strong electron-acoustic phonon coupling at the interface.

DOI: 10.1103/PhysRevB.93.195309

I. INTRODUCTION

The rise of thermoelectric efficiency in low-dimensional materials [1–8] is a longstanding source of inspiration for material design [9–15]. The potential of $LaAlO_3/SrTiO_3$ [16–21] and, more generally, of $SrTiO_3$-based heterostructures as thermoelectric materials stems from the early idea [1–3] (still controversial [6] and not clearly verified in experiments so far) that two-dimensional (2D) electron confinement could burst the already large thermoelectric power of the $SrTiO_3$ bulk, with room-temperature T Seebeck coefficient (S) of several hundredths μV/K in the low carrier density range $n \sim 10^{19}$ cm^{-3} [22,23]. In addition, with respect to the known Bi- and Te-based thermoelectric materials, oxides have the important advantage of being nontoxic and structurally compatible for integration in multifunctional heterostructures.

Remarkably large thermopower was reported for several 2D oxides. Most notably, an S up to ∼1000 μV/K, with a strong dependence on the carrier density, was measured in $SrTiO_3/SrTi_{0.8}Nb_{0.2}O_3$ superlattices [24–29]. Regarding $LaAlO_3/SrTiO_3$, the first measurement of the Seebeck coefficient in the range from $T = 77$ K to room-temperature T [30] gave values similar to those observed for low-doped $SrTiO_3$ bulk, but also revealed the possibility of tuning S by a gate voltage, as previously highlighted in the implementation of $SrTiO_3$-based transistors [31]. An anomalous low-T behavior of thermopower in $LaAlO_3/SrTiO_3$ was also reported [32]. The first S measurement in the extended $T = 4$–300 K range [33] revealed the presence of an impressively narrow and deep peak (∼500 μV/K) below $T = 50$ K, in striking contrast to the underlying diffusive regime which dictates a smooth and almost linear approach to zero with decreasing temperature. For assonance with the thermoelectric behavior of semiconductor-based quantum wells [34–36], it was logical to attribute the peak to the phonon-drag effect, i.e., the extra contribution to the electronic thermopower due to the drag of the electrons with the diffusing phonons, induced by the electron-phonon coupling. The presence of large phonon drag reappeared later in ion-gated $SrTiO_3$ [37] and in strongly charge-depleted $LaAlO_3/SrTiO_3$ [38], the latter in the form of spectacular Seebeck oscillations observed under negative gate field, with a Seebeck amplitude reaching record-high values of several tens mV/K, and attributed to the presence of localized states below the mobility edge.

In order to rationalize the general behavior of phonon drag and its sensitivity to the quantum confinement and localization, here we use a combination of experiments and modeling to perform a comparative analysis of phonon drag in several $LaAlO_3/SrTiO_3$ interfaces and doped $SrTiO_3$ crystals. We furnish clear evidence that for the interfaces, the low-T thermopower is dominated by a marked phonon-drag peak, which instead is absent (or barely detectable) in the bulk. Furthermore, we demonstrate that the phonon-drag peak is a consequence of the tight 2D electron confinement typical of oxide heterostructures. Indeed, in the low-temperature limit, the coupling of acoustic phonons with 2D-confined electrons is enhanced by the loss of the crystal momentum conservation in the interface-orthogonal direction, enabling the interaction of the electron gas with many more phonon frequencies. The close relation between strong electron-acoustic phonon scattering and large phonon drag was previously analyzed in $Al_xGa_{1-x}As/GaAs$ [39], MgZnO/ZnO [40], and carbon nanotubes [41]. For $LaAlO_3/SrTiO_3$, the huge phonon-drag peak can be understood as another manifestation of the strong electron-phonon coupling recently revealed by the polaronic nature of the two-dimensional electron system (2DES) [42], and also proposed to be the source of its superconducting behavior [43].

The paper is organized as follows: In Sec. II, we describe the experimental setup. Section III is devoted to the description of results, separated into thermoelectric and transport measurements (Sec. III A), measurements under field effect (Sec. III B), and theory results (Sec. III C). In Sec. IV, we draw our conclusions. Finally, in the Appendices, we describe the model used for our calculations in detail.

II. EXPERIMENTAL SETUP

$LaAlO_3/SrTiO_3$ interfaces are prepared by pulsed laser deposition. On a TiO_2-terminated (001)-oriented $SrTiO_3$ crystal, 5 unit cells (u.c.) (sample B) and 10 u.c. (samples A and C) of $LaAlO_3$ are grown at substrate temperature of 650° C (sample A) and 800° C (sample B and C) in an oxygen pressure of 10^{-5} mbar, and then annealed in an oxygen pressure of

200 mbar for one hour at 520° C before cooling down to room temperature in the same oxygen atmosphere [44]. A gold pad is evaporated on the back of the 0.5-mm-thick substrate and used as a gate electrode for field-effect experiments. Commercially available $SrTi_{1-x}Nb_xO_3$ single crystals with different Nb doping are also measured. The Seebeck coefficient is measured in a homemade cryostat, from 4 K to room temperature, using an ac technique [45]. A sinusoidal heating power with a period of 150 s is supplied to one side of the sample, producing a thermal gradient of 0.15 K/mm. Hall effect and resistivity data are measured in a PPMS system by Quantum Design, from 4 K to room temperature, in magnetic fields up to 9 Tesla.

III. RESULTS

A. Thermoelectric and transport measurements

Figure 1(a) displays the Seebeck coefficient measured as a function of T for the three different interface samples. We see that above 50–70 K, S is linear for all the samples, as expected in the diffusive regime. The linear slopes, varying between -0.37 and -1.28 $\mu V/K^2$, are reported in Table I, together with other measured transport quantities of the interfaces. Below 50 K, a sharp peak associated to the phonon-drag mechanism is observed. The temperature position of the peak is around 15–20 K in all of the cases, consistent with the fact that the maximum amplitude of the electron coupling with acoustic phonons is expected around $\theta_D/10$, if θ_D is the

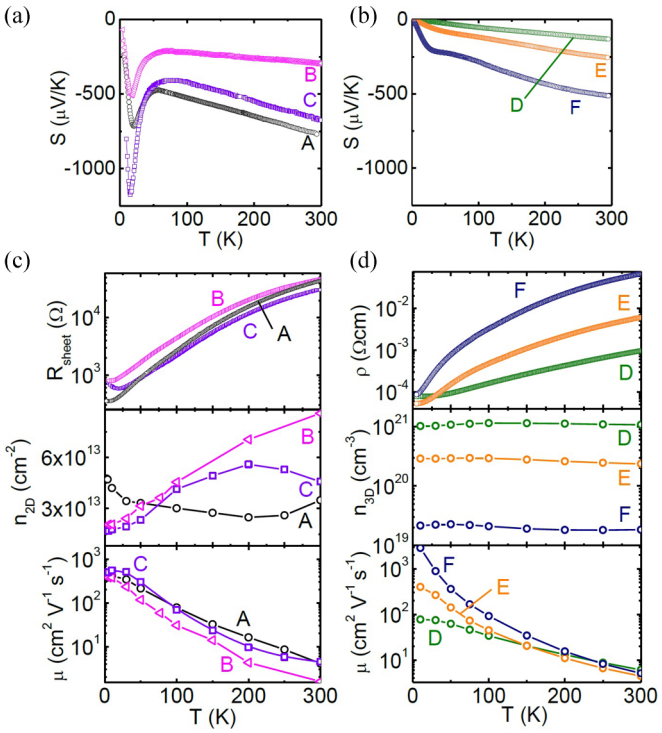

FIG. 1. (a) Seebeck coefficient S measured for the three interfaces as a function of temperature. (b) Seebeck coefficient for the three Nb-doped single crystals. (c) Sheet resistance (R_{sheet}), 2D carrier density (n_{2D}), and Hall mobility (μ) for the interfaces. (d) Resistivity (ρ), 3D carrier density (n_{3D}), and Hall mobility (μ) for the Nb-doped $SrTiO_3$ single crystals.

TABLE I. Some relevant transport parameters for our examined samples. From left to right: the S slope vs T in the linear (diffusive) regime ($\mu V/K^2$); S at room temperature ($\mu V/K$); the phonon-drag peak amplitude S_{peak} ($\mu V/K$); the Hall-measured carrier densities at $T = 4$ K (in cm^{-2} for the interfaces, cm^{-3} for bulks); the sheet resistance R_{sheet} for the interfaces (Ω) and the bulk resistivity ρ for the bulks (Ω cm) at $T = 4$ K; the Hall mobility at $T = 4$ K ($cm^2/V/s$).

LAO/STO	dS/dT	S	S_{peak}	n_{2D}	R_{sheet}	μ
A	−1.25	−770	−715	4.8×10^{13}	350	380
B	−0.37	−290	−500	2.0×10^{13}	800	380
C	−1.28	−680	−1180	1.7×10^{13}	740	560
STO	dS/dT	S	S_{peak}	n_{3D}	ρ	μ
D	−0.40	−134		1.0×10^{21}	7.85×10^{-5}	78
E	−0.73	−258	−62	2.9×10^{20}	5.25×10^{-5}	400
F	−1.20	−517	−210	2.2×10^{19}	8.65×10^{-5}	2870

Debye temperature (for undoped $SrTiO_3$ θ_D,~513 K [46]). At higher T, on the other hand, other phonon-scattering processes (namely, phonon-boundary scattering, phonon-impurity scattering, and phonon-phonon scattering) become dominant over electron-phonon scattering, and phonon drag rapidly fades. If the peak position is substantially the same in all of the samples, its amplitude is clearly sample dependent (see Table I), with a trend not trivially related to other fundamental characteristics such as carrier density, sheet resistance, or mobility (also reported in Table I): at low T, n_{2D} is rather similar for interfaces B and C, and a factor of two higher for A; consistently, R_{sheet} is nearly double for the former. Nevertheless, the highest phonon-drag peak occurs in C ($|S| \sim 1180$ $\mu V/K$) and the smallest in B ($|S| \sim 500$ $\mu V/K$), while A remains in the middle ($|S| \sim 715$ $\mu V/K$). The Hall mobility is also not very helpful in rationalizing the phonon-drag behavior: since a large phonon scattering due to defects or disorder plays in favor of phonon-drag suppression [47,48], it could be reasonable to expect a relation between low-T mobility and phonon drag. However, our data in Table I defy such a simple interpretation: samples A and B have the same mobility but quite a different drag peak. With the help of modeling, we will see later that the difference in amplitude can actually be traced back to different 2DES confinement thickness and planar charge localization, features not easily determined experimentally. The other transport quantities shown in Fig. 1(c) follow the expected behaviors: R_{sheet} increases with temperature and saturates to a residual, slightly sample-dependent value, the Hall-measured n_{2D} for all samples stays within the usual 10^{13}–10^{14} cm^{-2} range, and the Hall mobility decreases with increasing T.

In Fig. 1(b), we report the Seebeck coefficient measured for three Nb-doped $SrTiO_3$ bulk samples with different doping concentrations. Differently from the interfaces, they are essentially phonon-drag free, with the exception of the lowest-doped sample F, showing a minor deviation from the linear behavior in a form of a rounded shallow bump below 50 K. A barely visible inflection is also present for sample E. We can conclude that for bulk samples, phonon drag should be minor or smaller than the diffusive contribution. Notice also that the absence of phonon drag in $SrTiO_3$ crystals cannot

be merely attributed to the chemical doping, which would suppress the phonon relaxation time: for sample F, the mobility at low T is much higher than for the interfaces, and thus we may argue that for this sample, the electron-phonon vs impurity scattering ratio is larger than for the interfaces, and yet, there is no significant drag peak. Finally, in Fig. 1(d), the transport properties of the bulk samples are shown as a function of temperature. The resistivity curves can be phenomenologically described by the Bloch-Grüneisen law [49] plus a T^2 term [50]. The volume carrier densities n_{3D} are almost constant in the whole temperature range. For all three samples, n_{3D} is about three times as large as the nominal doping, indicating that some oxygen vacancies contribute to providing additional carriers. The mobility vs temperature curves are similar to those seen for the $SrTiO_3/LaAlO_3$ interfaces; the largest low-temperature value is reached for the least-doped compound (2870 $cm^2\,V^{-1}\,s^{-1}$ for sample F). The relevant transport parameters of the three single crystals are summarized in Table I.

B. Field-effect measurements

In Fig. 2, we report Seebeck coefficient measurements for interface sample A under a back-gate voltage V_g (no "poling protocol" is performed here [51]). We see that the phonon-drag peak is significantly modulated by the gate voltage. The asymmetry of S with respect to the sign of V_g is related to the nonlinear field dependence of the dielectric permittivity, and disappears above 77 K (see Ref. [30]) when permittivity no longer depends on the electric field. In the accumulation regime, V_g can be varied up to +200 V without detectable leakage and the magnitude of S at the phonon-drag peak (S_{peak}) is suppressed by only 5%. On the other hand, negative gate voltages are very effective in depleting the interface of carriers. For $V_g = -5$ V, we obtain a peak enhancement of 30%, while the diffusive regime at high temperature shows negligible modulation with the field, consistent with previous data [30]. The application of a negative V_g is known to produce a series of outstanding effects on the 2DES characteristics, related to charge depletion and increase of electron confinement [52]. In particular, Ref. [30] shows that negative gate fields of the order of MV/m can reduce the 2DES thickness up to a factor of two in the high-temperature regime $T > 77$ K. Thus, the large phonon-drag modulation by field effect is clear evidence that phonon drag is crucially related to the 2D extension of the gas.

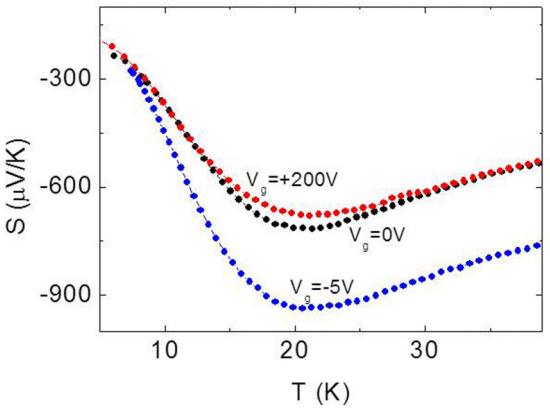

FIG. 2. Seebeck coefficient measured for interface sample A as a function of temperature for three values of the back-gate voltage V_g.

C. Phonon-drag modeling

To shed light on the phonon-drag mechanism at the fundamental level, we used the theory first developed by Bailyn [53] and then adapted to 2DES systems by Cantrell and Butcher [39–41,54–56], based on the Boltzmann transport equation (BTE) [57] for coupled electrons and phonons. To make the calculation affordable, we describe the 2DES electronic structure by an anisotropic effective mass modeling (previously used for a series of oxides [33,58–61]) and the acoustic phonon frequencies by a simple linear dispersion. Hereafter, we briefly sketch the final phonon-drag expression, leaving the detailed description for the Appendices. The phonon drag is

$$S_j^{\rm pd} = -\frac{e v_s^2}{(2\pi)^3 \sigma_j k_B T^2} \sum_n \sqrt{\frac{m_{nx}^* m_{ny}^*}{m_{nj}^{*\,2}}} \int_{\epsilon_n^0}^{\epsilon_n^0+W_n} d\epsilon\, f(\epsilon)\,\tau_n(\epsilon) \times \int_0^{q_0} dq_p\, q_p^3 \int_{-q_0}^{q_0} dq_z \frac{N_q[1-f(\epsilon+\hbar\omega_q)]}{\sqrt{C_{0,n}^2 - X_{0,n}^2}} \frac{A_n(q,q_z)}{\tau_{\rm ph}^{-1}(q)}, \quad (1)$$

where v_s is the speed of sound, σ_j is the 2D conductivity (in Ω^{-1}), m_{nj}^* is the effective mass of band n in direction j (x or y), ϵ is the electron energy, $f(\epsilon)$ and N_q are electron and phonon occupancies, respectively, $A_n(q,q_z)$ is the electron-phonon coupling amplitude, $\tau_n(\epsilon)$ and $\tau_{ph}(q)$ are electron and phonon relaxation times, respectively, ϵ_n^0 and W_n are band bottom and bandwidth, and $C_{0,n}$ and $X_{0,n}$ are the quantities depending on phonon and electron energy [see Eq. (A13) in Appendix A]. The integral over phonon wave vector $\mathbf{q}$ is solved in cylindrical coordinates, and $q_p = \sqrt{q_x^2 + q_y^2}$ and q_z are planar and orthogonal components, $q = \sqrt{q_p^2 + q_z^2}$. In Eq. (1), the crucial quantity which governs the phonon-drag magnitude is the ratio of electron-acoustic phonon coupling to phonon lifetime, with the former expressed as

$$A_n(q,q_z) = \tilde{A}(q) F_n(q_z), \quad F_n(q_z) = \left| \int_t dz\, \psi_n^2(z)\, e^{i q_z z} \right|^2, \quad (2)$$

where $\tilde{A}(q)$ includes the deformation potential and the piezoelectric contributions [39], and $\psi_n(z)$ is the wave function of the 2D-confined electrons, whose Fourier transform F_n governs the coupling of 3D phonons with the electrons confined along z within a slice of thickness t. In the $t \to \infty$ limit, $F_n \to \delta_{q_z,0}$, i.e., only zero-wavelength phonons can couple with electrons, and the coupling amplitude goes back to the 3D case, where $\mathbf{q}$ is fully determined by the crystal momentum conservation $\mathbf{k}' = \mathbf{k} + \mathbf{q}$. In the case of infinite confinement ($t = 0$), on the other hand, all q_z up to the Debye wavelength do contribute to the coupling, and $F_n = 1$. Regarding $\tau_{\rm ph}(q)$, we use the low-temperature modeling developed by Callaway [62] [see Eq. (A17) in Appendix A], while band structure parameters m_{nj}^*, ϵ_n^0, and W_n are taken from our previous *ab initio* results [33,63].

In the calculation, we want to put in evidence the key features which govern the phonon-drag amplitude: the gas thickness t, the in-plane localization (thus m^*_{nj}), and the n_{2D} charge density. Those are all quite difficult to be precisely determined in the experiments, since they are crucially affected by a number of hard-to-control conditions such as structural disorder, oxygen vacancies, and cation intermixing. Exploiting the flexibility of band modeling, we thus treat them as variable parameters to explore the phonon-drag behavior in a range of different conditions. Regarding the 2DES thickness, *ab initio* results [33,63–72] show that for the charge density of interest ($\sim$2–4 $\times$ 10^{13} cm^{-2}), the gas is entirely included in a few ($\sim$2–3) d_{xy} states confined in the TiO_2 layers closest to the interface, while only above $\sim 6 \times 10^{13}$ cm^{-2} do the more extended d_{xz}, d_{yz} states set in. However, in order to evaluate the scaling with respect to the 2D confinement, it is convenient to replace the actual squared wave functions with Gaussian envelope functions of variable thickness t (see Appendix A for details). In Fig. 3, we show three sets of phonon-drag calculations relative to different values of effective masses and n_{2D}, each of them for variable t from a single unit cell up to 100 nm (i.e., in the bulk limit). Figure 3(a) shows the phonon drag for masses derived from *ab initio* calculations ($m^*_x = m^*_y =$ $0.7m_e$ for d_{xy} states) which represent the "clean" interface limit, while Fig. 3(b) is obtained using "fattened" effective masses ($1.4m_e$ for d_{xy}) mimicking an increased in-plane charge localization, typically associated with structural distortions and disorder. Finally, in Fig. 3(c), we use "ideal" masses and an increased n_{2D} [notice that the explicit mass dependence in Eq. (1) vanishes for isotropic masses, but the most crucial mass dependence is implicitly included in $f(\epsilon)$ through the Fermi energy]. In Fig. 3, we also report the diffusive Seebeck coefficient, sheet resistance, and mobility calculated by BTE for the different masses and densities, and $t = 1$ nm.

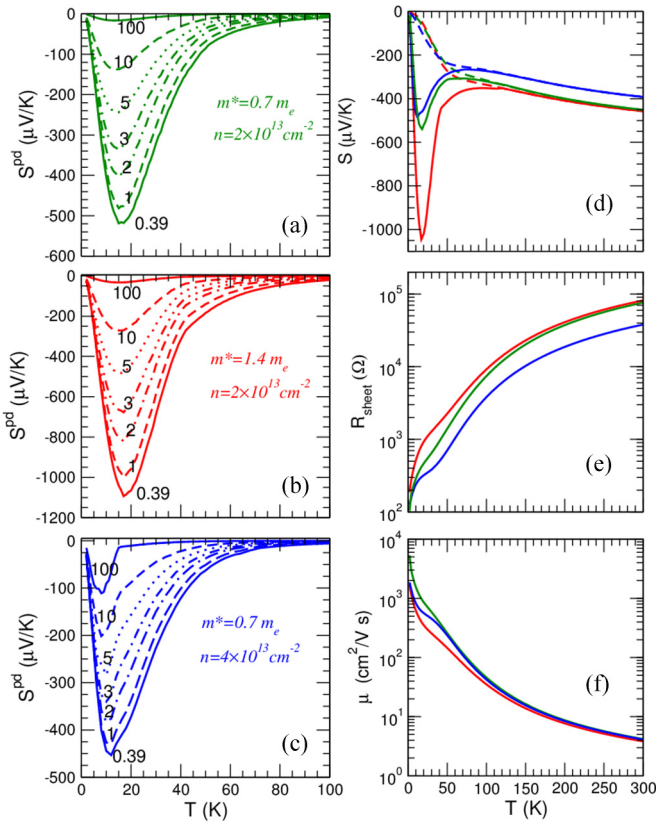

FIG. 3. (a)–(c) Model calculation of phonon drag vs temperature at varying gas thickness t (indicated for each line in nm). Each panel corresponds to different values of effective masses and charge densities, also reported on each panel. (d) Diffusive Seebeck coefficient (dashed lines) and total (diffusive plus phonon-drag) Seebeck coefficient (full lines) for the three sets of calculations and $t = 1$ nm. Green curves are for case (a), red curves for (b), and blue curves for (c). (e) Sheet resistance; (f) electron mobility.

Overall, a good match with the observations is obtained. Our phonon-drag values qualitatively reproduce the major features observed in the experiment: the phonon drag appears as a sharp peak centered at $T \sim 20$ K, and for $T > 50$ K, it disappears behind the diffusive Seebeck coefficient. The peak amplitude crucially depends on both 2DES thickness and effective masses. In fact, we see that only for thickness of $\sim$10 nm or less, the phonon-drag peak becomes significantly visible above the low-temperature diffusive background. In particular, assuming as maximum possible confinement the thickness of a single unit cell ($t = 0.39$ nm), we obtain peaks higher than 500 and 1000 μV/K for the two sets of masses, which are in the range of the values observed for the interfaces. More complicated is tracing the phonon-drag dependence on the charge density: a larger charge implies higher Fermi energy, but also more occupied bands (i.e., more bands actively contributing to the phonon drag). The net result is t dependent: for weakly confined 2DES, the second aspect prevails and the phonon drag increases with the density. In the narrow-thickness limit, the two effects nearly compensate and phonon drag is slightly larger for the lower density. Overall, the effect of a pure charge filling on the phonon drag appears to be weaker than confinement and localization. Clearly, in actual cases, these three ingredients (thickness, localization, and density) are tightly interlaced with each other, and thus a fine-tuned interpretation of the differences observed among the interface samples is cumbersome. What is significant in the simulation, on the other hand, is that assuming realistic values for n_{2D}, the phonon-drag scaling with thickness and effective masses spans the whole range of measured values, from the bulk to the tightly confined 2DES regime.

IV. CONCLUSIONS

In conclusion, we report the measured thermopower for several $LaAlO_3/SrTiO_3$ interfaces in comparison with that of Nb-doped $SrTiO_3$ crystal samples. We give evidence that for the interfaces, thermopower below 50 K is dominated by a high phonon-drag peak, reaching huge values of the order of $\sim$mV/K. On the other hand, phonon drag is substantially absent, or barely apparent, in bulks. With the help of numerical modeling, we traced back the presence of such a large phonon-drag peak to the tight 2D confinement of the 2DES and to the charge localization at the interface: specifically, the 2D thickness establishes the cutoff on the wavelength of the acoustic phonons which can couple to the confined electrons, while planar localization crucially controls the Fermi energy and, in turn, the phonon-drag amplitude. From our analysis, phonon drag emerges as a remarkable marker of charge

localization and confinement in 2D heterostructures, and a significant parameter of classification for 2DES systems in general.

ACKNOWLEDGMENTS

This work is supported by the Italian MIUR through Project FIRB RBAP115AYN (Oxides at the nanoscale, multifunctionality and applications) and PRIN 2010NR4MXA (OXIDE); the Swiss National Science Foundation through the Thermoelectric Oxides (TEO) project and Division II, and the European Research Council under the European Unions Seventh Framework Programme (FP7/20072013)/ERC Grant Agreement No. 319286 (Q-MAC). A.F. acknowledges computational support from the CRS4 Computing Center (Piscina Manna, Pula, Italy).

APPENDIX A: PHONON-DRAG MODELING IN 2D

We follow the original Cantrell-Butcher (CB) formulation [55,56] for the expression of phonon drag in 2D heterostructures. The theory is developed starting from the Boltzmann transport equation within relaxation-time approximation for a coupled system of 3D acoustic phonons and 2D electrons. Using the same CB notations, assuming intraband scattering only, the phonon drag in direction $j = (x, y)$ can be expressed as

$$S_j^{\rm pd} = \left(\frac{2e}{\sigma_j A k_B T^2}\right) \sum_{nk,nk',q} \hbar\omega_q \left[\frac{\Gamma_{nk,nk'}(\mathbf{q})}{\tau_{\rm ph}^{-1}(\mathbf{q})}\right] \times v_j(\mathbf{q})[\tau(n\mathbf{k}) v_j(n\mathbf{k}) - \tau(n\mathbf{k}') v_j(n\mathbf{k}')], \quad \text{(A1)}$$

with A the unit area, σ_j the 2D conductivity (in Ω^{-1}), $\mathbf{q} = (q_x, q_y, q_z)$ and $k = (k_x, k_y)$ the phonon and electron crystalline momenta, $\tau_{\rm ph}(\mathbf{q})$ and $\tau(n\mathbf{k})$ the phonon and electron relaxation times, $v_j(\mathbf{q})$ and $v_j(n\mathbf{k})$ the phonon and electron velocities, and $\Gamma_{nk,nk'}(\mathbf{q})$ the electron-acoustic phonon-scattering rate,

$$\Gamma_{nk,nk'}(\mathbf{q}) = f_{n\mathbf{k}}(1 - f_{n\mathbf{k}'}) N_{\mathbf{q}} A_n(\mathbf{q}) \times \delta(\epsilon_{n\mathbf{k}'} - \epsilon_{n\mathbf{k}} - \hbar\omega_{\mathbf{q}}) \delta_{\mathbf{k}',\mathbf{k}+\mathbf{q}_p}, \quad \text{(A2)}$$

where $f_{n\mathbf{k}}$ and $N_{\mathbf{q}}$ are electron and phonon occupancies, $A_n(\mathbf{q})$ is the coupling amplitude, and the two δ functions account for energy and in-plane momentum conservation [$\mathbf{q}_p = (q_x, q_y)$]. Notice that Eq. (A2) is written for the absorption process, but emission is implicitly accounted for in Eq. (A1). In Ref. [56], Eq. (A1) is made treatable assuming linear phonon dispersion and parabolic band modeling for electrons. Here we follow the same strategy, except for the generalization to anisotropic band masses in the plane, which better describes the t_{2g} states of the 2DES. It is easy to see that

$$v_j(\mathbf{q})[\tau_{n\mathbf{k}} v_j(n\mathbf{k}) - \tau(n\mathbf{k}') v_j(n\mathbf{k}')] = -\frac{\hbar v_s}{m_{nj}^*} \frac{q_j^2}{q} \tau(n\mathbf{k}), \quad \text{(A3)}$$

where m_{nj}^* is the effective mass of the nth band in direction j; also, for simplicity, we assume $\tau(n\mathbf{k}) = \tau(n\mathbf{k}')$. Notice that the minus sign in Eq. (A3) comes from the fact that for positive band curvature (electrons), the band velocity increases with $\mathbf{k}$; it follows that phonon drag is negative for electrons, just like diffusive thermopower. In order to treat anisotropic bands, we introduce the following change of in-plane $j = (x, y)$ variables:

$$k_j = K_j \sqrt{\frac{m_{nj}^*}{m}}, \quad q_j = Q_j \sqrt{\frac{m_{nj}^*}{m}}, \quad \text{(A4)}$$

where m is an auxiliary mass which, using in-plane momentum conservation, allows one to write

$$\epsilon_{n\mathbf{k}} = \frac{\hbar^2 K^2}{2m}, \quad \epsilon_{n,\mathbf{k}+\mathbf{q}_p} = \epsilon_{n,\mathbf{K}+\mathbf{Q}} = \frac{\hbar^2(\mathbf{K}+\mathbf{Q})^2}{2m}, \quad \text{(A5)}$$

$$\delta(\epsilon_{\mathbf{K}+\mathbf{Q}} - \epsilon_{\mathbf{K}} - \hbar\omega_{\mathbf{q}}) = \delta\left(\frac{\hbar^2 Q^2}{2m} + \frac{\hbar^2 K Q \cos\theta}{m} - \hbar\omega_{\mathbf{q}}\right), \quad \text{(A6)}$$

where θ is the angle formed by $\mathbf{K}$ and $\mathbf{Q}$. It is convenient to introduce another variable change,

$$X = \frac{\hbar^2 K Q}{m} \cos\theta = C_0 \cos\theta, \quad X_0 = \hbar\omega_q - \frac{\hbar^2 Q^2}{2m}. \quad \text{(A7)}$$

Then, we solve the sum over $\mathbf{K}$ in 2D for a fixed $\mathbf{K}$ in radial coordinates, taking the azimuth angle to be that formed by $\mathbf{K}$ and $\mathbf{Q}$. It is easy to see that

$$d\theta = -dX \frac{1}{\sqrt{C_0^2 - X^2}}, \quad K\,dK = \frac{m}{\hbar^2} d\epsilon_K, \quad \text{(A8)}$$

$$\sum_k \delta(\epsilon_{\mathbf{K}+\mathbf{Q}} - \epsilon_{\mathbf{K}} - \hbar\omega_{\mathbf{q}}) = \frac{A}{(2\pi)^2\hbar^2} \sqrt{m_{nx}^* m_{ny}^*} \int d\epsilon \int_{X\in[-C_0,C_0]} dX \frac{\delta(X - X_0)}{\sqrt{C_0^2 - X^2}}. \quad \text{(A9)}$$

The argument of the square root is always positive, since $X \in [-C_0, C_0]$. To have a nonvanishing integral in dX, it must be $-C_0 \leqslant X_0 \leqslant C_0$, i.e.,

$$\frac{\hbar^2(\mathbf{K}-\mathbf{Q})^2}{2m} \leqslant \epsilon_{n\mathbf{k}} + \hbar\omega_{\mathbf{q}} \leqslant \frac{\hbar^2(\mathbf{K}+\mathbf{Q})^2}{2m}, \quad \text{(A10)}$$

which has a simple interpretation: after absorption, the carrier energy must be higher (lower) than the band energy corresponding to antiparallel (parallel) $\mathbf{K}$ and $\mathbf{Q}$ orientation. We have

$$\int_{X\in[-C_0,C_0]} dX \frac{\delta(X - X_0)}{\sqrt{C_0^2 - X^2}} = \frac{2}{\sqrt{C_0^2 - X_0^2}}. \quad \text{(A11)}$$

Since $\theta \in [0, 2\pi]$, there are always two values [$\cos(\theta_0)$ and $\cos(-\theta_0)$] for which the δ function is nonvanishing. Inserting Eq. (A2) in Eq. (A1), solving for the energy-conserving δ function according to Eqs. (A9) and (A11), and using $\omega_{\mathbf{q}} = v_s q$, the phonon drag in 2D becomes

$$S_j^{\rm pd} = -\frac{4e v_s^2 V}{(2\pi)^5 \sigma_j k_B T^2} \sum_n \sqrt{\frac{m_{nx}^* m_{ny}^*}{(m_{nj}^*)^2}} \int d^3q\, q_j^2 \frac{N_{\mathbf{q}} A_n(\mathbf{q})}{\tau_{\rm ph}^{-1}(\mathbf{q})} \times \int_{\epsilon_n^0}^{\epsilon_n^0 + W_n} d\epsilon\, f_\epsilon(1 - f_{\epsilon+\hbar\omega_q}) \tau_n(\epsilon) \frac{1}{\sqrt{C_{0,n}^2 - X_{0,n}^2}}, \quad \text{(A12)}$$

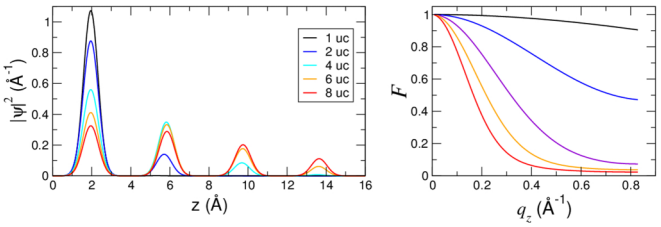

FIG. 4. Left panel: z-localized squared wave functions with varying localization length, normalized to unity. Right: corresponding Fourier transforms. Each wave function is built as a sum of Gaussian functions, centered in the middle of a perovskite unit cell, further interpolated by a Gaussian envelope of varying thickness.

$$C_{0,n}^2 = \frac{2\hbar^2\tilde{q}_n^2}{m_{nx}^* m_{ny}^*}\epsilon_K, \quad X_{0,n} = \hbar\omega_q - \frac{\hbar^2\tilde{q}_n^2}{2m_{nx}^* m_{ny}^*}, \quad \text{(A13)}$$

where $\tilde{q}_n^2 = q_x^2\, m_{ny}^* + q_y^2\, m_{nx}^*$. In 2D, the electron-acoustic phonon-scattering amplitude can be written at the simplest level of approximation [73],

$$A_n(q,q_z) = \left[C_{\rm DP}\, q + C_{\rm PZ}\frac{q^3}{(q^2+q_D^2)^2}\right]F_n(q_z), \quad \text{(A14)}$$

$$C_{\rm DP} = \frac{\pi D^2}{V\rho v_s}, \quad C_{\rm PZ} = \frac{\pi e^2 v_s K_{\rm em}^2}{V k_0 k}, \quad \text{(A15)}$$

$$F_n(q_z) = \left|\int_t dz\, \psi_n^2(z)\, e^{iq_z z}\right|^2. \quad \text{(A16)}$$

$C_{\rm DP}$ and $C_{\rm PZ}$ account for deformation potential and piezoelectric scattering, respectively. D is the deformation potential, ρ is the mass density, k_0 and k are vacuum permittivity and dielectric constant, $K_{\rm em}$ is the 3D-averaged electromechanical coupling, q_D is the Debye screening length, and $\psi_n(z)$ is the space-localized wave function of the scattered electrons. The deformation-potential term describes the coupling of electrons with longitudinal acoustic waves treated as a homogeneous strain. The piezoelectric scattering is the additional contribution due to the coupling with the electric field produced by the strain. For a nonpolar system ($K_{\rm em} = 0$) or in the limit of large doping concentration (i.e., strong Debye screening), the second term vanishes and only the deformation potential contributes to the acoustic scattering. In the case of small screening ($q_D = 0$) and highly ionic compounds, on the other hand, the piezoelectric contribution ($\sim 1/q$) may become dominant at small q. Assuming a very long Debye screening length ($q_D \sim 0$), screening becomes discardable and the electron-phonon scattering increases [36], i.e., in the low-density charge-localized limit, carrier mobility is so small that the piezoelectric interaction becomes unscreened. In the case of $LaAlO_3/SrTiO_3$, both terms are relevant and should be included in the treatment.

In the form factor F_n, we assume the same initial and final wave function for the scattered carrier. This is reasonable since F_n depends weakly on the specific wave-function shape; what matters the most is its overall extension, i.e., the thickness t of the well. In Fig. 4, we show the relation between a series of normalized squared wave functions obtained by a superposition of Gaussian functions, with localization length progressively increased from one to eight unit cells, and the corresponding Fourier transforms F_n. In the case of maximum localization, the entire charge is enclosed in a single unit cell (black line) and the corresponding F_n weight is about unity, i.e., all of the phonons with q_z up to the Debye wavelength ($q_z \sim 0.83$ Å^{-1} in $SrTiO_3$) contribute to the scattering; for a squared wave function localized in 8 u.c. (about 31 Å in $SrTiO_3$), on the other hand, only phonons with $q_z > 0.2$ Å^{-1} contribute. In the limit of complete delocalization, ($t \to \infty$) is $F_n \to \delta(q_z,0)$. Thus, the 2DEG confinement is a major factor of phonon-drag amplification in oxide heterostructures, as discussed in the main text.

Finally, for the phonon-relaxation time, we use the Callaway formula [62],

$$\tau_{\rm ph}^{-1} = A\,\omega_q^4 + B\,T^3\omega_q^2 + \frac{v_s}{L}, \quad \text{(A17)}$$

including scattering by point impurities (first term), phonon-phonon scattering (second term), and boundary scattering (third term; here, L is a characteristic sample length; in our model, $L = 1$ mm). In our calculations, A and B are adjusted to have a phonon-drag value in the bulk limit ($t \to \infty$), which is small with respect to the diffusive Seebeck, consistent with what is observed in the experiments. Then these values are kept fixed, while t is progressively reduced, in order to describe the scaling effect purely due to the confinement thickness on the phonon-drag amplitude.

APPENDIX B: APPROXIMATE SOLUTIONS FOR THE PHONON-DRAG INTEGRATION IN 2D

Using the series of Eqs. (A12)–(A17), phonon drag can be obtained by numerical integration and evaluated at any given temperature and doping. However, this requires the integration over four coupled coordinates (three for the phonon wave vector and one for the electron energy). To reduce the computational weight, we can follow two routes:

(a) *Isotropic 2D approximation*. In plane, we take $q_j^2 \sim 1/2\, q_p^2$. It follows that the arguments of the square root in Eq. (A11) become dependent on two coordinates only, and the integral over q can be expressed in cylindrical coordinates. Thus phonon drag is reduced to a three-variable integration:

$$S_j^{\rm pd} = -\frac{e v_s^2}{(2\pi)^3\sigma_j k_B T^2}\sum_n \sqrt{\frac{m_{nx}^* m_{ny}^*}{(m_{nj}^*)^2}}\int_{\epsilon_n^0}^{\epsilon_n^0+W_n} d\epsilon f_\epsilon\, \tau_n(\epsilon)$$
$$\times \int_0^{q_0} dq_p\, q_p^3 \int_{-q_0}^{q_0} dq_z\, \frac{N_q}{\tau_{\rm ph}^{-1}(q)}\frac{(1-f_{\epsilon+\hbar\omega_q})}{\sqrt{C_{0,n}^2 - X_{0,n}^2}}$$
$$\times\left[C_{\rm DP}q + C_{\rm PZ}\frac{q^3}{(q^2+q_D^2)^2}\right]F_n(q_z), \quad \text{(B1)}$$

which corresponds to Eq. (1) and was actually used for our calculations. Here, $\pi q_0^2 = (2\pi)^2/A$ and $q_0 = 2\sqrt{\pi}/a_0$. Also,

electron and phonon energies must obey the constraints

$$\hbar\omega_q \leqslant \frac{\hbar^2 q_p^2}{2\tilde{m}} + \hbar q_p \sqrt{\frac{2\epsilon_{nk}}{\tilde{m}}}, \tag{B2}$$

$$\hbar\omega_q \geqslant \frac{\hbar^2 q_p^2}{2\tilde{m}} - \hbar q_p \sqrt{\frac{2\epsilon_{nk}}{\tilde{m}}}, \tag{B3}$$

with

$$\tilde{m}_n = \frac{2m^*_{nx}m^*_{ny}}{m^*_{nx}+m^*_{ny}}. \tag{B4}$$

(b) *Small phonon frequencies*. In the case of small phonon energies and low T, the following equation holds (adopted in the CB work):

$$f_\epsilon(1-f_{\epsilon+\hbar\omega_q}) \sim \frac{\hbar\omega_q}{1-e^{-\frac{\hbar\omega_q}{k_B T}}} = \hbar\omega_q(N_q+1)\delta(\epsilon-\epsilon_F). \tag{B5}$$

Thus, in Eq. (A12), the electron energy integral can be factorized and solved, and the phonon drag becomes only dependent on phonon coordinates,

$$S_j^{\rm pd} = -\frac{2e\nu_s^2}{(2\pi)^4\sigma_j k_B T^2}\sum_n \sqrt{\frac{m^*_{nx}m^*_{ny}}{(m^*_{nj})^2}}\tau_n(\epsilon_F) \times \int d^3q\, q_j^2 \left[\frac{\hbar\omega_q N_q(N_q+1)}{\tau_{\rm ph}^{-1}(q)\sqrt{C^2_{0,n}(\epsilon_F)-X^2_{0,n}}}\right] \times \left[C_{\rm DP}\, q + C_{\rm PZ}\frac{q^3}{(q^2+q_D^2)^2}\right]F_n(q_z), \tag{B6}$$

with

$$C^2_{0,n}(\epsilon_F) = \frac{2\hbar^2\tilde{q}_n^2}{m^*_{nx}m^*_{ny}}\epsilon_F, \quad X_{0,n} = \hbar\omega_q - \frac{\hbar^2\tilde{q}_n^2}{2m^*_{nx}m^*_{ny}}. \tag{B7}$$

The approaches (a) and (b) give results to within 10–15% from each other in the fully converged limit of electron energy and phonon wave-vector integration. The results shown in Fig. 3 are obtained using Eq. (B1).

APPENDIX C: VALUES OF PARAMETERS USED FOR THE CALCULATION

Several parameters entering the phonon-drag modeling are unknown or difficult to calculate for $LaAlO_3/SrTiO_3$; in this case, we rely on values appropriate for $SrTiO_3$. For the phonon drag, we use $\nu_s = 7.9\times10^5$ cm/s, $k = 300$, $D = 8$ eV, $K_{\rm em} = 0.35$; for the phonon relaxation time, we use $A = 0.5\times10^{-41}$ (adimensional), $B = 0.5\times10^{-20}$ K^{-3}, and $L = 0.1$ mm. The electronic band structure is described by a multiband effective mass modeling, including three t_{2g} bands for each unit cell, with masses $(m_x^*, m_y^*) = (0.7,0.7)m_e$ for d_{xy}, $(0.7,8.8)m_e$ for d_{xz}, and $(8.8,0.7)m_e$ for d_{yz}. The band bottoms ϵ_n^0 are scaled according to the *ab initio* band structure calculations at varying charge density [63]: for the d_{xy} states, $\epsilon_1^0 = 0$, $\epsilon_2^0 = 20$ meV, $\epsilon_{i+1}^0 = 30$ meV, for $i = 2,3,4,\ldots$ (i is the number of u.c. distance from the interface); for the d_{xz} and d_{yz} states, we take $\epsilon_i^0 = 30$ meV for each i since they are substantially spread within the substrate and their confinement along z is discardable for charge densities $n_{\rm 2D} \sim 10^{13}$ cm^{-2}. Finally, for the calculation of diffusive Seebeck and conductivity, we use the same formulation and parameters previously adopted in Refs. [33] and [38].

[1] L. D. Hicks, T. C. Harman, and M. S. Dresselhaus, Appl. Phys. Lett. **63**, 3230 (1993).
[2] L. D. Hicks and M. S. Dresselhaus, Phys. Rev. B **47**, 16631 (1993).
[3] L. D. Hicks and M. S. Dresselhaus, Phys. Rev. B **47**, 12727 (1993).
[4] D. A. Broido and T. L. Reinecke, Phys. Rev. B **51**, 13797 (1995).
[5] L. D. Hicks, T. C. Harman, X. Sun, and M. S. Dresselhaus, Phys. Rev. B **53**, R10493 (1996).
[6] G. D. Mahan and J. O. Sofo, Proc. Natl. Acad. Sci. USA **93**, 7436 (1996).
[7] M. Dresselhaus, G. Chen, M. Tang, R. Yang, H. Lee, D. Wang, Z. Ren, J.-P. Fleurial, and P. Gogna, Adv. Mater. **19**, 1043 (2007).
[8] J. O. Sofo and G. D. Mahan, Appl. Phys. Lett. **65**, 2690 (1994).
[9] R. Venkatasubramanian, E. Siivola, T. Colpitts, and B. O'Quinn, Nature (London) **413**, 597 (2001).
[10] A. Majumdar, Science **303**, 777 (2004).
[11] G. J. Snyder and E. S. Toberer, Nat. Mater. **7**, 105 (2008).
[12] K. Biswas, J. He, I. D. Blum, C. I. Wu, T. P. Hogan, D. N. Seidman, V. P. Dravid, and M. G. Kanatzidis, Nature (London) **489**, 414 (2012).
[13] M. Zebarjadi, K. Esfarjani, M. S. Dresselhaus, Z. F. Ren, and G. Chen, Energy Environ. Sci. **5**, 5147 (2012).
[14] D. G. Cahill, P. V. Braun, G. Chen, D. R. Clarke, S. Fan, K. E. Goodson, P. Keblinski, W. P. King, G. D. Mahan, A. Majumdar, H. J. Maris, S. R. Phillpot, E. Pop, and L. Shi, Appl. Phys. Rev. **1**, 011305 (2014).
[15] M. Beekman, D. T. Morelli, and G. S. Nolas, Nat. Mater. **14**, 1182 (2015).
[16] A. Ohtomo and H. Y. Hwang, Nature (London) **427**, 423 (2004).
[17] M. Huijben, G. Rijnders, D. H. Blank, S. Bals, S. Van Aert, J. Verbeeck, G. Van Tendeloo, A. Brinkman, and H. Hilgenkamp, Nat. Mater. **5**, 556 (2006).
[18] W. Siemons, G. Koster, H. Yamamoto, W. A. Harrison, G. Lucovsky, T. H. Geballe, D. H. A. Blank, and M. R. Beasley, Phys. Rev. Lett. **98**, 196802 (2007).
[19] N. Nakagawa, H. Y. Hwang, and D. A. Muller, Nat. Mater. **5**, 204 (2006).
[20] N. Reyren, S. Thiel, A. D. Caviglia, L. Kourkoutis, G. Hammerl, C. Richter, C. W. Schneider, T. Kopp, A.-S. Rüetschi, D. Jaccard, M. Gabay, D. A. Muller, J.-M. Triscone, and J. Mannhart, Science **317**, 1196 (2007).
[21] J. Mannhart and D. G. Schlom, Science **327**, 1607 (2010).
[22] T. Okuda, K. Nakanishi, S. Miyasaka, and Y. Tokura, Phys. Rev. B **63**, 113104 (2001).

[23] S. Ohta, T. Nomura, H. Ohta, and K. Koumoto, J. Appl. Phys. **97**, 034106 (2005).

[24] Y. Mune, H. Ohta, K. Koumoto, T. Mizoguchi, and Y. Ikuhara, Appl. Phys. Lett. **91**, 192105 (2007).

[25] H. Ohta, S. Kim, Y. Mune, T. Mizoguchi, K. Nomura, S. Ohta, T. Nomura, Y. Nakanishi, Y. Ikuhara, M. Hirano, H. Hosono, and K. Koumoto, Nat. Mater. **6**, 129 (2007).

[26] H. Ohta, Mater. Today **10**, 44 (2007).

[27] H. Ohta, Y. Mune, K. Koumoto, T. Mizoguchi, and Y. Ikuhara, Thin Solid Films **516**, 5916 (2008).

[28] H. Ohta, Phys. Status Solidi B **245**, 2363 (2008).

[29] H. Ohta, R. Huang, and Y. Ikuhara, Phys. Stat. Sol. (RRL) **2**, 105 (2008).

[30] I. Pallecchi, M. Codda, E. Galleani d'Agliano, D. Marré, A. D. Caviglia, N. Reyren, S. Gariglio, and J.-M. Triscone, Phys. Rev. B **81**, 085414 (2010).

[31] H. Ohta, Y. Masuoka, R. Asahi, T. Kato, Y. Ikuhara, H. Nomura, and K. Hosono, Appl. Phys. Lett. **95**, 113505 (2009).

[32] S. Lerer, M. Ben Shalom, G. Deutscher, and Y. Dagan, Phys. Rev. B **84**, 075423 (2011).

[33] A. Filippetti, P. Delugas, M. J. Verstraete, I. Pallecchi, A. Gadaleta, D. Marré, D. F. Li, S. Gariglio, and V. Fiorentini, Phys. Rev. B **86**, 195301 (2012).

[34] R. Fletcher, J. J. Harris, C. T. Foxon, M. Tsaousidou, and P. N. Butcher, Phys. Rev. B **50**, 14991 (1994).

[35] R. Fletcher, Y. Feng, C. T. Foxon, and J. J. Harris, Phys. Rev. B **61**, 2028 (2000).

[36] R. Fletcher, M. Tsaousidou, P. Coleridge, Y. Feng, and Z. Wasilewski, Physica E **12**, 478 (2002).

[37] S. Shimizu, S. Ono, T. Hatano, Y. Iwasa, and Y. Tokura, Phys. Rev. B **92**, 165304 (2015).

[38] I. Pallecchi, F. Telesio, D. Li, A. Fête, S. Gariglio, J.-M. Triscone, A. Filippetti, P. Delugas, V. Fiorentini, and D. Marré, Nat. Commun. **6**, 6678 (2015).

[39] M. Tsaousidou, P. N. Butcher, and G. P. Triberis, Phys. Rev. B **64**, 165304 (2001).

[40] M. Tsaousidou, Phys. Status Solidi RRL **7**, 554 (2013).

[41] M. Tsaousidou, Phys. Rev. B **81**, 235425 (2010).

[42] C. Cancellieri, A. S. Mishchenko, U. Aschauer, A. Filippetti, C. Faber, O. S. Barišić, V. A. Rogalev, T. Schmitt, N. Nagaosa, and V. N. Strocov, Nat. Commun. **7**, 10386 (2016).

[43] B. Rosenstein, Y. B. Shapiro, I. Shapiro, and D. Li, arXiv:1601.07425.

[44] C. Cancellieri, N. Reyren, S. Gariglio, A. D. Caviglia, A. Fête, and J.-M. Triscone, Europhys. Lett. **91**, 17004 (2010).

[45] V. Calzona, M. R. Cimberle, C. Ferdeghini, M. Putti, and A. S. Siri, Rev. Sci. Instrum. **64**, 766 (1993).

[46] M. Ahrens, R. Merkle, B. Rahmati, and J. Maier, Physica B **393**, 239 (2007).

[47] A. B. Kaiser, Phys. Rev. B **35**, 4677 (1987).

[48] S. Chatterjee, P. K. Pal, S. Bhattacharya, and B. K. Chaudhuri, Phys. Rev. B **58**, 12427 (1998).

[49] E. Grüneisen, Ann. Phys. (Leipzig) **408**, 530 (1933).

[50] D. van der Marel, J. L. M. van Mechelen, and I. Mazin, Phys. Rev. B **84**, 205111 (2011).

[51] Note that hysteretic effects for different thermal and gate voltage cycles appear at large negative V_g and low temperature, as remarked in previous works [J. Biscaras *et al.*, arXiv:1206.1198; J. Biscaras *et al.*, Sci. Rep. **4**, 6788 (2014)]. A stable electrostatic confinement can be obtained by a suitable poling protocol, as long as the system is maintained at low temperature. However, in this work, we do not carry out any poling protocol and we investigate the reversible regime at higher temperature, so that we observe no hysteresis as the temperature increases above ∼10 K.

[52] J. Biscaras, N. Bergeal, S. Hurand, C. Grossetête, A. Rastogi, R. C. Budhani, D. LeBoeuf, C. Proust, and J. Lesueur, Phys. Rev. Lett. **108**, 247004 (2012).

[53] M. Bailyn, Phys. Rev. **157**, 480 (1967).

[54] D. G. Cantrell and P. N. Butcher, J. Phys. C **19**, L429 (1986).

[55] D. G. Cantrell and P. N. Butcher, J. Phys. C **20**, 1985 (1987).

[56] D. G. Cantrell and P. N. Butcher, J. Phys. C **20**, 1993 (1987).

[57] P. B. Allen, in *Quantum Theory of Real Materials*, edited by J. R. Chelikowsky and S. G. Louie (Kluwer, Boston, 1996), p. 219.

[58] P. Delugas, A. Filippetti, A. Gadaleta, I. Pallecchi, D. Marré, and V. Fiorentini, Phys. Rev. B **88**, 115304 (2013).

[59] P. Delugas, A. Filippetti, M. J. Verstraete, I. Pallecchi, D. Marré, and V. Fiorentini, Phys. Rev. B **88**, 045310 (2013).

[60] P. Delugas, V. Fiorentini, A. Mattoni, and A. Filippetti, Phys. Rev. B **91**, 115315 (2015).

[61] D. Puggioni, A. Filippetti, and V. Fiorentini, Phys. Rev. B **86**, 195132 (2012).

[62] J. Callaway, Phys. Rev. **113**, 1046 (1959).

[63] C. Cancellieri, M. L. Reinle-Schmitt, M. Kobayashi, V. N. Strocov, P. R. Willmott, D. Fontaine, P. Ghosez, A. Filippetti, P. Delugas, and V. Fiorentini, Phys. Rev. B **89**, 121412 (2014).

[64] R. Pentcheva and W. E. Pickett, Phys. Rev. B **74**, 035112 (2006).

[65] M. S. Park, S. H. Rhim, and A. J. Freeman, Phys. Rev. B **74**, 205416 (2006).

[66] J. Lee and A. A. Demkov, Phys. Rev. B **78**, 193104 (2008).

[67] Z. S. Popović, S. Satpathy, and R. M. Martin, Phys. Rev. Lett. **101**, 256801 (2008).

[68] R. Pentcheva and W. E. Pickett, Phys. Rev. B **78**, 205106 (2008).

[69] R. Pentcheva and W. E. Pickett, Phys. Rev. Lett. **102**, 107602 (2009).

[70] K. Janicka, J. P. Velev, and E. Y. Tsymbal, Phys. Rev. Lett. **102**, 106803 (2009).

[71] P. Delugas, A. Filippetti, V. Fiorentini, D. I. Bilc, D. Fontaine, and P. Ghosez, Phys. Rev. Lett. **106**, 166807 (2011).

[72] M. Stengel, Phys. Rev. Lett. **106**, 136803 (2011).

[73] B. K. Ridley, *Quantum Processes in Semiconductors* (Clarendon, Oxford, 1999).